Fatigue Crack Path and Threshold in Mode II and Mode III Loadings

Y. Murakami[1], Y. Fukushima[1], K. Toyama[2] and S. Matsuoka[1]

[1] Department of Mechanical Engineering Science, Kyushu University, 744 Motooka, Nishi-ku, Fukuoka, 819-0395, Japan, ymura@mech.kyusyu-u.ac.jp
[2] Forensic Science Laboratory, Fukuoka Prefectural Police Headquarters, 7-7 Higashi-Koen, Hakata-ku, Fukuoka, 812-8576, Japan.

ABSTRACT. *In order to investigate the crack path under Mode II or Mode III loadings, reversed torsion tests were carried out on SAE52100 and Mode II fatigue crack growth tests were carried out on 0.47 % carbon steel specimens. In the torsional fatigue test (SAE52100), the type of inclusion in the torsional fatigue fracture origin was slender MnS inclusions which are elongated in the longitudinal direction. The cracks first propagated by Mode II up to crack length 2a = 100 ~ 200 μm (which are almost equal to the length of MnS inclusion) in the longitudinal direction, and then branched by Mode I to the direction (~ ± 70.5 deg.) perpendicular to the local maximum normal stress ($\sigma_{\theta max}$) at the crack tip.*

In the Mode II fatigue crack growth test (0.47 % carbon steel) in air and in a vacuum, the cracks first propagated by Mode II. After the Mode II fatigue crack growth stopped, the crack branched to the direction perpendicular to the local maximum normal stress ($\sigma_{\theta max}$) at the crack tip, and finally branched to the angle close to the direction perpendicular to the remote maximum principal stresses.

A fibrous pattern on the Mode II fatigue fracture surface tested in a vacuum was clearer than that in air. The Mode II threshold stress intensity factor ranges, ΔK_{IIth} = 10.2 MPa $\sqrt{m}$ (Longitudinal crack) and ΔK_{IIth} = 12.5 MPa $\sqrt{m}$ (Transverse crack) in a vacuum were higher than those in air, ΔK_{IIth} = 9.4 MPa $\sqrt{m}$ (Longitudinal crack) and ΔK_{IIth} = 10.8 MPa $\sqrt{m}$ (Transverse crack). Both in a vacuum and in air, the values of ΔK_{IIth} for crack growth perpendicular to the rolling direction were higher than those for crack growth parallel to the rolling direction.

The values of K_{II} and K_{III} at a 3D elliptical crack tip under shear stress were analyzed to investigate the shear crack growth pattern in materials. The 3D crack analysis shows that the most stable aspect ratio b/a of a small planar elliptical crack under cyclic shear stress is b/a = 0.49 in absence of friction at crack surfaces. The aspect ratio b/a = 0.49 can be explained by the equal resistance against fatigue crack growth both in Mode II and Mode III, i.e. $\Delta K_{IIth} = \Delta K_{IIIth}$. However, the aspect ratio b/a for the failure of a real railway wheel did not stay at the stable aspect ratio b/a = 0.49 and continued

decreasing. The cause for the decrease in the aspect ratio b/a smaller than 0.49 was revealed to be the friction between crack surfaces.

INTRODUCTION

Mode II fatigue failure occurs in several components such as bearings, gears, rails, rolls, etc., as the damage types of shelling, spalling and pitting. The origins of the Mode II fatigue crack are surface or subsurface of components. Mode II fatigue crack starting from surface propagates in air or with lubricant. Mode II fatigue crack initiating from subsurface inclusions is thought to propagate in a vacuum. It has been reported that in Mode I fatigue crack growth, the crack growth behaviour in air is different from that in a vacuum [1-5]. Kikukawa et al. [2] and Jono et al. [3] reported that the Mode I crack growth threshold ΔK_{Ith} in a vacuum was higher than that in air and the crack growth resistance was increased in a vacuum. McEvily et al. [4] reported that the crack tip opening displacement (CTOD) in a vacuum is larger than that in air due to the lack of oxidation. Thus, the Mode II fatigue crack growth behaviours in a vacuum can also be different from those in air.

In this study, the Mode II fatigue crack path and the threshold value ΔK_{IIth} under Mode II loading and Mode II + III crack growth under torsional fatigue loading were studied. The influence of a vacuum environment on the Mode II fatigue threshold and a 3D shear crack growth behaviours under Mode II and Mode III loading were also investigated.

EXPERIMENTAL PROCEDURES

Torsional fatigue test

Table 1 shows the chemical composition of a bearing steel, SAE52100. The Vickers hardness, measured with a load 0.98 N, is HV = 797. The scatter of HV measured at 12 points is within 11%.

Figure 1 shows the shape and dimensions of the torsional fatigue test specimen. After finishing the specimen surface with emery paper, the surface layer was removed by electro-polishing. A hydraulically controlled biaxial fatigue testing machine was used. Tests were conducted under load control at a frequency of 0.1 ~ 0.2 Hz. Crack paths were measured by using replica method.

Table 1. Chemical composition of SAE52100 (wt. %)

C	Si	Mn	P	S	Ni	Cr	Mo	Cu	Al	Ti	O (ppm)
0.992	0.27	0.39	0.015	0.005	0.08	1.4	0.03	0.11	0.008	0.030	6

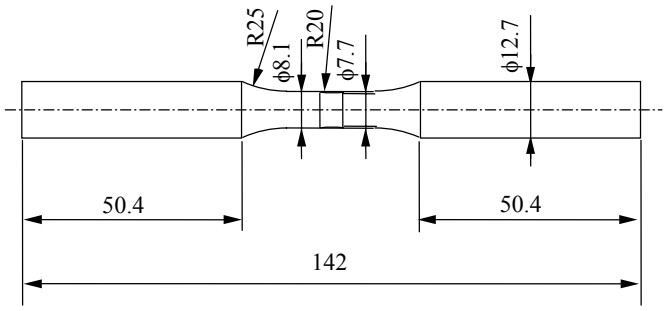

Figure 1. Torsional fatigue test specimens (mm).

Mode II fatigue crack growth test in a vacuum

In comparison with the Mode II fatigue crack growth behaviours in air [10-12], Mode II fatigue crack growth tests in a vacuum were conducted by using 0.47% carbon steel.

Table 2 shows the chemical composition of the 0.47 % carbon steel. Specimens were machined after annealing at 844°C, for 1h. After turning specimen, the specimens were annealed in a vacuum at 600°C for 1h to relieve the residual stress introduced by turning. The Vickers hardness after vacuum annealing is HV = 196. The scatter of HV measured at 4 points is within 5 %.

Figure 2(a) shows the shape and dimensions of the Mode II fatigue crack growth test specimen. The Mode II fatigue crack growth tests were conducted by using the specially designed double cantilever (DC) type specimen designed by Murakami and Hamada [6-8]. The specimen has a chevron notch and side grooves in the slit. This specimen enables ΔK_{II}-decreasing test under a constant load amplitude. Two series of specimen were prepared. One is for Mode II fatigue crack growth parallel to the rolling directions (Longitudinal crack) and another is for Mode II fatigue crack growth perpendicular to the rolling directions (Transverse crack).

Figure 2(b) shows the Mode II fatigue test system in a vacuum. A conventional tension-compression fatigue testing machine was used with a pair of the specimens. Test method details are given in Ref. [6-8]. Tests were conducted at a constant load amplitude, ΔP = 11.8 kN with R = -1 and at a frequency of 6 Hz. In order to conduct the Mode II fatigue crack growth test in a vacuum, the vacuum chamber was installed to the fatigue testing machine. An oil sealed rotary pump and turbo-molecular pump were used to make a vacuum condition. The maximum vacuum pressure in the chamber is about 2×10^{-3} Pa.

Table 2. Chemical composition of 0.47 % carbon steel (wt. %)

	C	Si	Mn	P	S	Cr	Cu	Ni
Mode II specimen	0.47	0.20	0.67	0.010	0.04	0.04	0.01	0.02

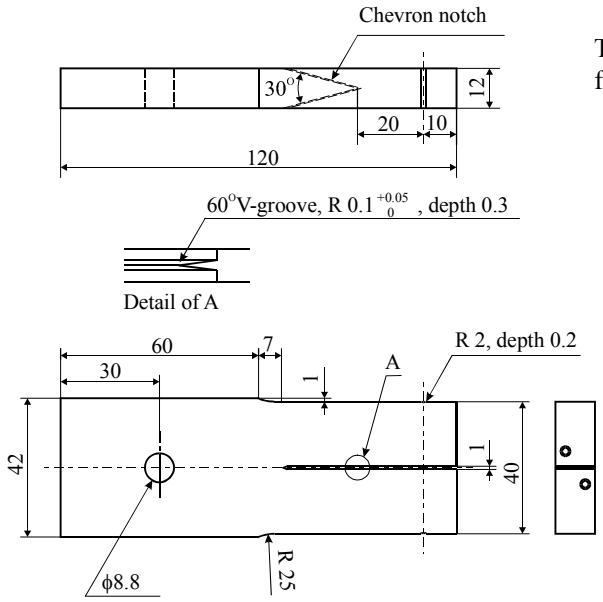

(a) Mode II fatigue test specimens (mm).

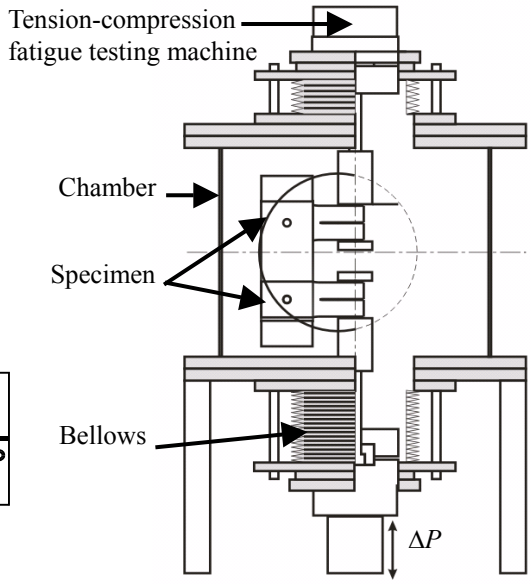

(b) Mode II fatigue test system.

Figure 2. Mode II fatigue crack growth test in a vacuum.

Results and Discussions

Fatigue crack path under the reversed torsion (Mode III loadings)

Figure 3 shows the crack initiation and propagation from slender inclusions under the reversed torsion. The nominal shear stress amplitude τ is defined by $16T/\pi d^3$ though yielding occurs on the specimen surface. After the Mode II fatigue crack grew on the specimen surface along the axial direction, the Mode II fatigue crack growth branched by the Mode I crack growth. The Mode I branched cracks continued propagation and led the specimen to failure.

Table 3 shows the branched angles from Mode II to Mode I. Mode II crack lengths $2a$ increased with increasing τ. The branched angles are close to the direction (± 70.5 deg.) perpendicular to the local maximum normal stress ($\sigma_{\theta max}$). This result is similar to those reported in Ref. [9]. It must be noted that the discussion on the branching angle at the crack tip under Mode II loading is not so simple because of the problem of the corner point singularity of 3D crack [13]. The analytically predicted angle of crack propagation from an elliptical hole under shear stress is ± 45 deg., even if the ellipse becomes very slender like a crack. This contradiction is discussed in Appendix [17].

Table 3. Branch angles from Mode II to Mode I (μm, deg.)

τ (MPa)	$2a$	θ_1	θ_2	θ_3	θ_4
1200	93	-	-	-	-
1200	100	70	60	63	50
1300	200	51	65	47	53
1400	225	-	58	63	76

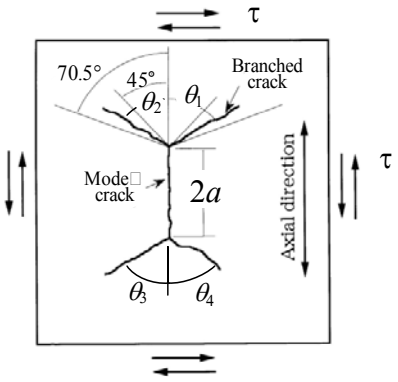

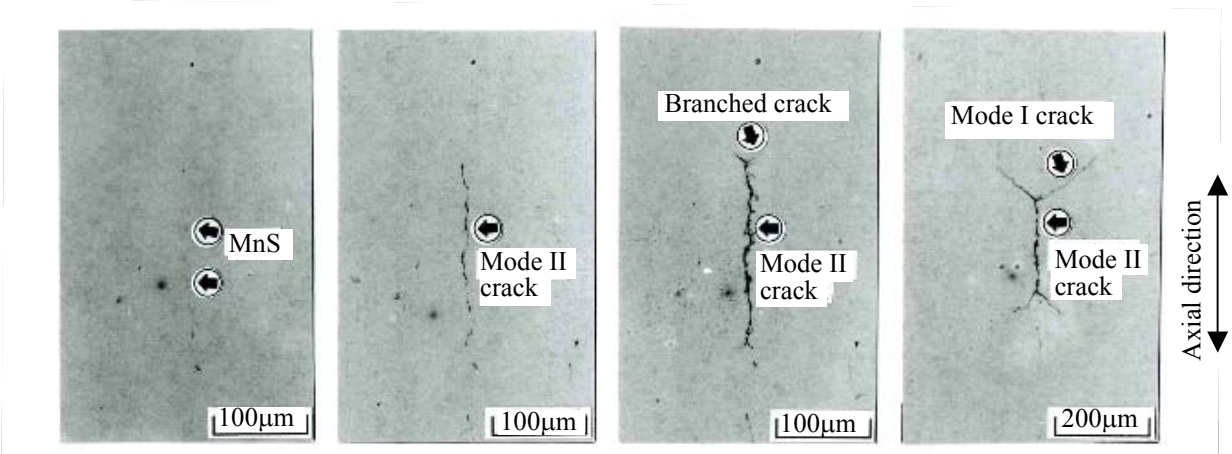

(a) $N = 0$ (b) $N = 1000$ (c) $N = 1500$ (d) $N = 1750$

Figure 3. Crack initiation from MnS inclusions and propagation under torsional fatigue, $\tau = 1300$ MPa, $N_f = 1760$ (SAE52100).

Fatigue crack path under Mode II fatigue loadings

Figure 4 shows a side view of the Mode II fatigue crack that was revealed by sectioning the Mode II fatigue crack growth test specimen along its central section. The sectioned plane of the specimen tested in a vacuum was etched with a nital. In both tests in air and in a vacuum, the fatigue crack first grew by Mode II. As the Mode II fatigue crack grows, the value of the ΔK_{II} decreases. After ΔK_{II} reached the threshold value ΔK_{IIth}, the crack branched by Mode I. The branched angles ± 70.5 deg. are the value calculated by the local maximum normal stress criterion ($\sigma_{\theta max}$) [14] and the branched angle close to ± 45 deg. is the direction perpendicular to the remote maximum principal stress σ_1. The side view of the Mode II fatigue crack in a vacuum was thinner than that in air. This is due to the lack of oxidation in a vacuum.

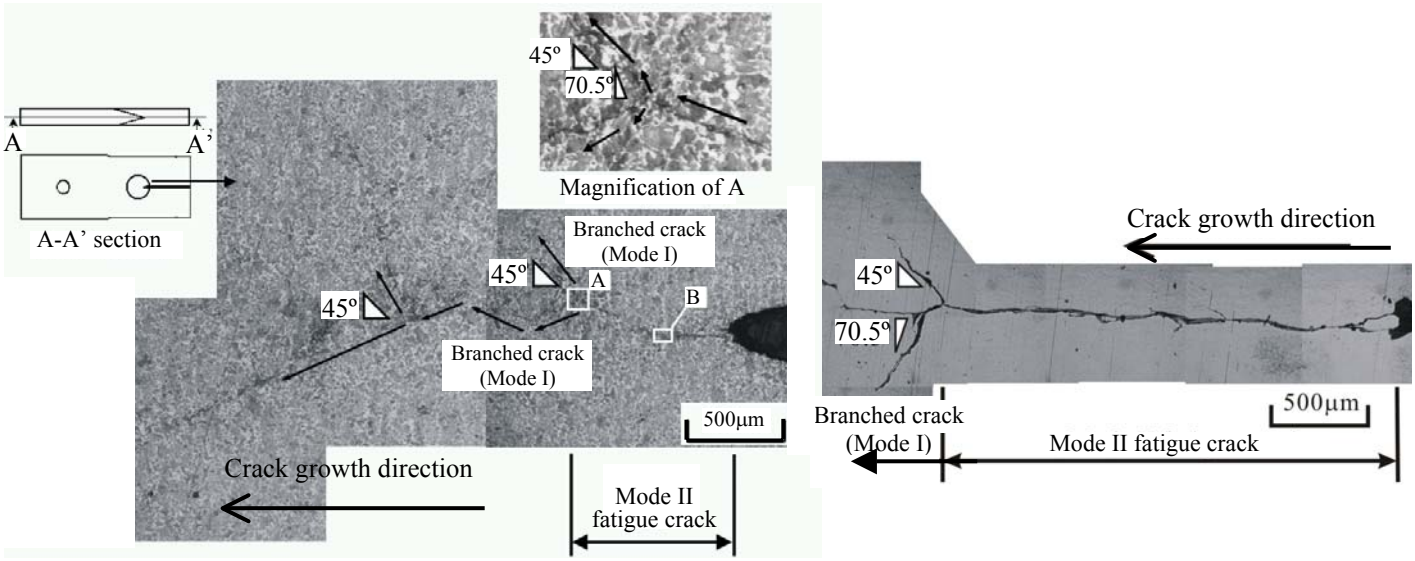

(a) Mode II fatigue crack profile in a vacuum. (b) Mode II fatigue crack profile in air [12].

Figure 4. Mode II fatigue crack profile in air and in a vacuum.

Mode II fatigue crack growth threshold ΔK_{IIth}

In order to decide Mode II fatigue crack growth threshold ΔK_{IIth} in air and in a vacuum, the relationship between Mode II fatigue crack length and ΔK_{II} were investigated by the finite element method (FEM).

Figure 5(a) shows the shape and dimensions of FEM model. Material properties are Young's modulus, E = 206GPa and Poisson ratio, ν = 0.3. The Mode II crack lengths a are 0.3, 0.6, 2.0 and 5.0 mm and the assumed friction coefficient μ during Mode II fracture surfaces are 0.0, 0.2, 0.4, 0.6, 0.8 and 1.0.

Figure 5(b) shows the variation of K_{II} in terms of crack length a. K_{II} were calculated by stress distribution singularity at the Mode II crack tip. Mode II stress intensity factor K_{II} decreases as the Mode II crack length a increases. And, the K_{II} decreases as friction coefficient μ increases. In order to decide the Mode II crack growth threshold ΔK_{IIth} by FEM results and the Mode II fatigue crack length, the friction coefficient μ must be determined. The friction coefficient in air was set to μ = 0.6 considering the results of the preview studies [8].The friction coefficient in a vacuum is unknown. We need to estimate it. The friction coefficient in a vacuum is higher than that in air. Moreover, in Mode I crack, ΔK_{Ith} in a vacuum is higher than that in air [3]. The crack length for Mode II fatigue threshold in a vacuum is shorter than that in air. Considering all these data, the friction coefficient in a vacuum could be assumed to be $\mu \approx 0.7$. Thus, the values of ΔK_{IIth} in a vacuum was determined to be μ = 0.7.

Table 4 shows the Mode II crack length a and ΔK_{IIth} in air and in a vacuum. The Mode II threshold stress intensity factor ranges in a vacuum were higher than those in air. The values of ΔK_{IIth} for crack growth perpendicular to the rolling direction (Transverse crack) were higher than those for crack growth parallel to the rolling direction (Longitudinal crack). The reason for higher values of ΔK_{IIth} in a vacuum is due to the lack of oxidation at crack surfaces in a vacuum. It is presumed that new surfaces of the Mode II fatigue crack tip in a vacuum may be easily re-adhered.

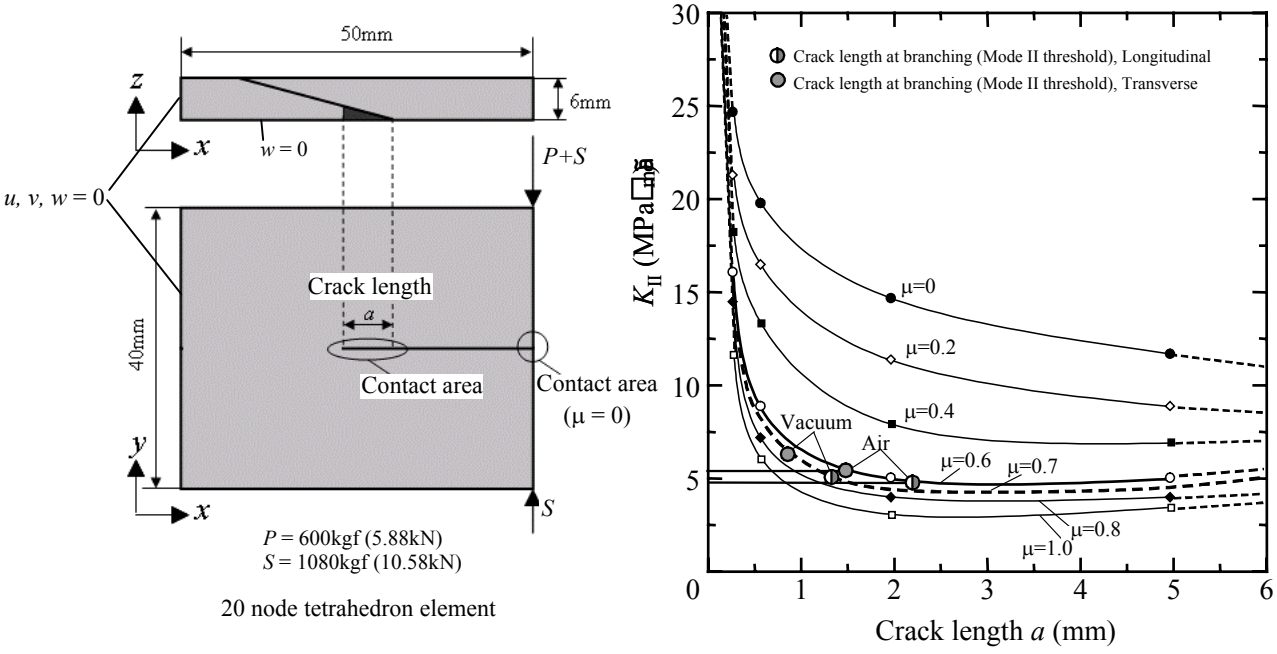

(a) Analysis model and boundary condition. (b) Relationship between Mode II crack length a and Mode II stress intensity factor K_{II}.

Figure 5. FEM model and analysis result.

Table 4. Mode II crack growth threshold, ΔK_{IIth} and crack length a (0.47 % carbon steel)

ΔK_{IIth} (MPa$\sqrt{\text{m}}$) and a (mm)

	ΔK_{IIth} (a) in air	ΔK_{IIth} (a) in a vacuum
Transverse crack	10.8 (1.47mm)	12.5 (0.84mm)
Longitudinal crack	9.4 (2.15mm)	10.2 (1.30mm)

Fractographs

Figure 6 (a) shows the torsional fatigue fracture surface of the SAE52100. The slender inclusion in the fracture origin was a MnS. The trace of the inclusion was observed at the fracture origin. The length of the MnS inclusions in the fracture origin is approximately equal to the Mode II fatigue crack length on the specimen surface.

Figure 6 (b) shows the Mode III fracture surface (Magnification of Fig.6 (a) where fatigue crack growth in the depth direction is Mode III). The particular feature of the fracture surface is fibrous patterns parallel to the direction of shear stress. On the specimen surface, the crack branched at the edge of the inclusion at the fracture origin. As the branched crack grows, the fatigue crack growth in Mode II becomes difficult. Eventually, the contour of the Mode III fatigue crack is deepened (See Fig. 6 (c)) although the stable aspect ratio b/a for a planar elliptical crack under shear stress is 0.49 as shown in the next section (Fig. 11).

Figure 7 (a) and (b) show the Mode II fracture surface of the 0.47 % carbon steel tested in air and in a vacuum by the test of Fig.2. In both in air and in a vacuum, fibrous patterns parallel to the direction of shear stress were observed.

Figure 8 (a) and (b) are the comparison between the fracture surface in the Mode II fatigue test in air and that observed at the fracture accident of a real steel making roll. The fracture origin of the real roll was at a subsurface and accordingly the Mode II crack propagated in the material without exposure to air until the final fracture accident occurred. Fibrous pattern on the Mode II fatigue fracture surface for the specimen tested in a vacuum was clearer than that in air in both the 0.47 % carbon steel and the roll steel (SKD6). The difference of the appearance between the Mode II fracture surfaces in air and in a vacuum both for Fig. 7 (a) and (b), and also Fig. 8 (a) and (b) is due to the production of the oxide layer on the fracture surface in air.

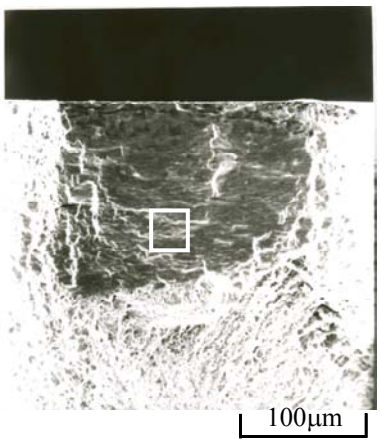

(a) Fracture surface.

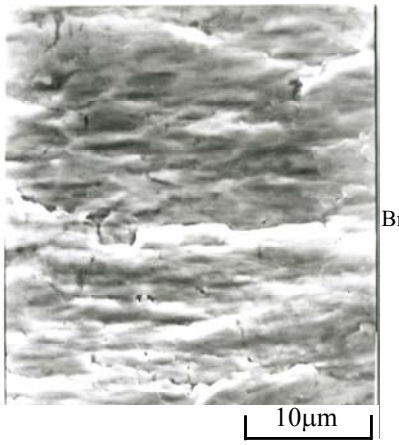

(b) Magnification of (a).

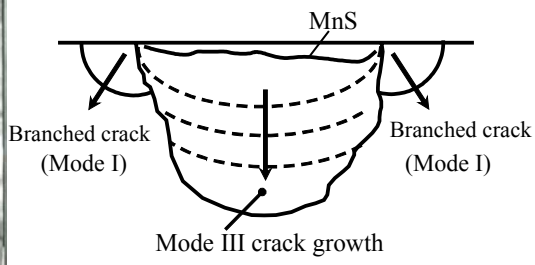

(c) The contour of the Mode III fatigue crack.

Figure 6. Fracture surface in the vicinity of the fracture origin in the torsional fatigue. τ = 1300MPa, N_f = 1760, l_{max} = 68μm

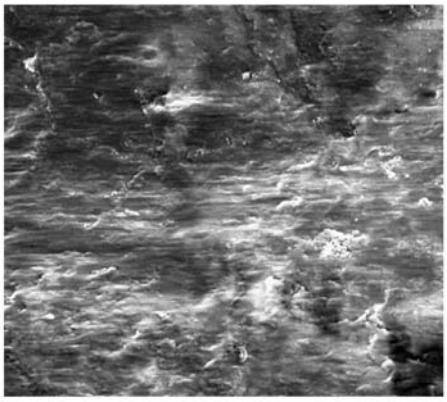

(a) Mode II fatigue fracture surface in air [10,11].

(b) Mode II fatigue fracture surface in a vacuum.

Figure 7. Mode II fatigue fracture surface, 0.47% C steel.

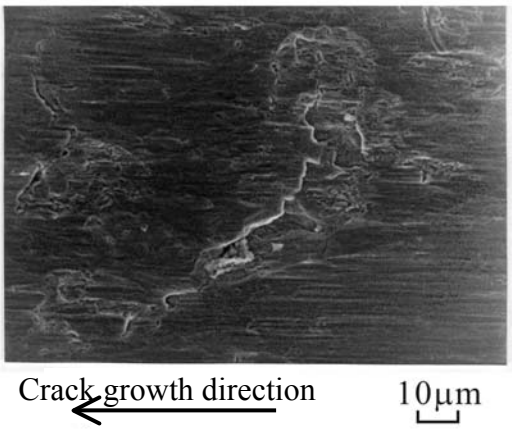

(a) Mode II fatigue fracture surface in air.

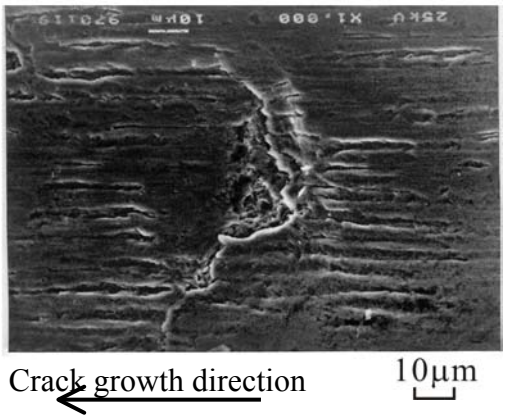

(b) Fracture surface of a real roll.

Figure 8. Mode II fatigue fracture surface of a roll steel, SKD6.

Analysis of 3D shear crack growth behaviours

In order to determine the 3D crack propagation pattern under Mode II and Mode III loading, it is necessary to understand the material resistance against Mode II and Mode III crack growth. Murakami et al. [10-12] made clear that ΔK_{IIth} is essentially equal to ΔK_{IIIth}, i.e. $\Delta K_{IIth} = \Delta K_{IIIth}$. It implies that a 3D planar crack grows with the condition that the relationship $K_{II} = K_{III}$ is satisfied. The values of K_{II} and K_{III} for a 3D elliptical crack in an infinite body under shear stress were calculated by using Kassir et al.'s solution [15].

Figure 9 shows a 3D elliptical crack in an infinite body under shear stress. The leading edge of the major axis of the elliptical crack (point A) is at the condition of the pure Mode II. On the other hand, the edge of the minor axis of the elliptical crack (point B) is the condition of the pure Mode III. We assume that the elliptical crack grows

under the condition of ΔK_{II} (point A) = ΔK_{III} (point B). Now, the value of K_{II} for the leading edge of the major axis of the elliptical crack (point A) is expressed for $b < a$ by

$$K_{II} = \left(\frac{\pi b^3}{a}\right)^{1/2} \frac{k^2 \tau \sin\beta}{\left[\left(k^2 - \nu\right)E(k) + \nu k'^2 K(k)\right]\left(b^2 \sin^2\beta + a^2 \cos^2\beta\right)^{1/4}}$$

$$= \left(\frac{\pi b^3}{a}\right)^{1/2} \frac{k^2 \tau}{\left[\left(k^2 - \nu\right)E(k) + \nu k'^2 K(k)\right](b)^{1/2}} \quad \cdots\cdots\cdots\cdots\cdots\cdots (1)$$

Similarly, the value of K_{III} for the edge of the minor axis of elliptical crack (point B) is expressed for $b < a$

$$K_{III} = (\pi ab)^{1/2} \frac{-(1-\nu)k^2 \tau \cos\beta}{\left[\left(k^2 - \nu\right)E(k) + \nu k'^2 K(k)\right]\left(b^2 \sin^2\beta + a^2 \cos^2\beta\right)^{1/4}}$$

$$= (\pi ab)^{1/2} \frac{-(1-\nu)k^2 \tau}{\left[\left(k^2 - \nu\right)E(k) + \nu k'^2 K(k)\right](a)^{1/2}} \quad \cdots\cdots\cdots\cdots\cdots\cdots (2)$$

Where,

$$k = \left(1 - \frac{b^2}{a^2}\right)^{1/2}, \; k' = \frac{b}{a}$$

$$E(k) = \int_0^{\pi/2} \left(1 - k^2 \sin^2\phi\right)^{1/2} d\phi,$$

$$K(k) = \int_0^{\pi/2} \frac{d\phi}{\left(1 - k^2 \sin^2\phi\right)^{1/2}}$$

Here, we assume $\nu = 0.3$.

From Eqs. (1) and (2), we can derive the aspect ratio (b/a) which satisfies the condition of ΔK_{II} (point A) = ΔK_{III} (point B), is $b/a = 0.49$.

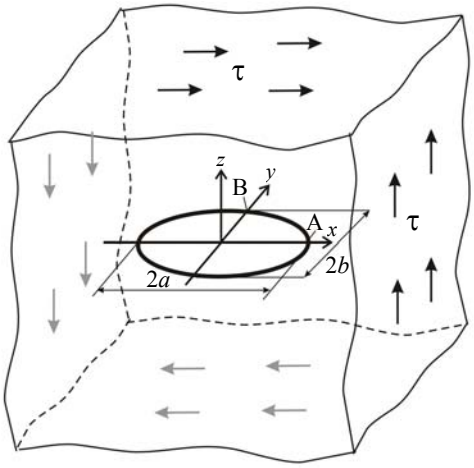

Figure 9. A 3D elliptical crack in an infinite body under shear stress [15].

Figure 10 shows the fracture surface of a real railway wheel [16] reported by Beretta et al.. The fracture surface is parallel to the external surface of the wheel. The origin of the fracture surface is a Al_2O_3 cluster inclusions aligned in the rolling direction. Firstly, the fatigue crack propagates in not only in the rolling direction but also in the direction perpendicular to the rolling direction and eventually become a circular shape crack (Phase 1). This stage of crack growth is promoted by Mode I under the residual tensile stress produced by the cyclic compression load. After this stage, the crack grows by Mode II and Mode III (Phase 2). Eventually, the planar elliptical crack grows toward the aspect ratio 0.49 under cyclic shear stress. However, the aspect ratio continued decreasing as shown in Fig. 10 (b). The cause for the decrease in the aspect ratio b/a smaller than 0.49 was assumed to be the friction between crack surfaces and the effect of friction was investigated by the FEM in the following.

Figure 11 shows the FEM model for an elliptical crack with the aspect ratio b/a = 0.49. Material properties are assumed as Young's modulus, E = 206GPa and Poisson ratio, ν = 0.3. Here, it must be noted that the crack size is much larger than the half contact width from the situation of Fig. 10.

Figure 12 shows the variation of K_{II} at the leading edge of the major axis of the elliptical crack with the aspect ratio b/a = 0.49 (point A) and K_{III} at the edge of the minor axis of the elliptical crack with the aspect ratio b/a = 0.49 (point B). For the friction coefficient between the crack surfaces, μ = 0.0, ΔK_{II} at the leading edge of the major axis of the elliptical crack (point A) is approximately equal to ΔK_{III} at the edge of the minor axis of the elliptical crack (point B). However, for the friction coefficient between the crack surfaces, μ = 0.5, ΔK_{II} at the leading edge of the major axis of the elliptical crack (point A) is higher than ΔK_{III} at the edge of the minor axis of the elliptical crack (point B). Thus, it may be concluded that the friction between crack surfaces causes the smaller aspect ratio of the 3D elliptical crack than 0.49.

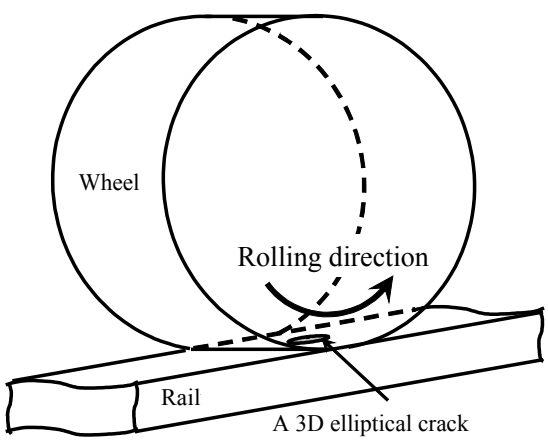

(a) Railway wheel.

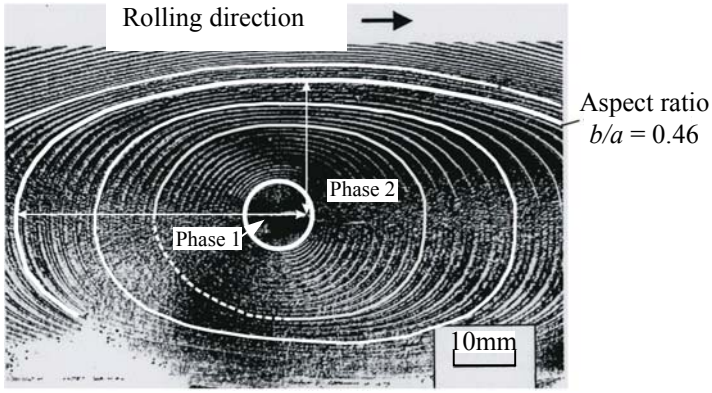

(b) A 3D elliptical crack growth pattern in a real railway wheel.

Figure 10. A 3D elliptical crack growth pattern in a real railway wheel, Beretta et al. [16].

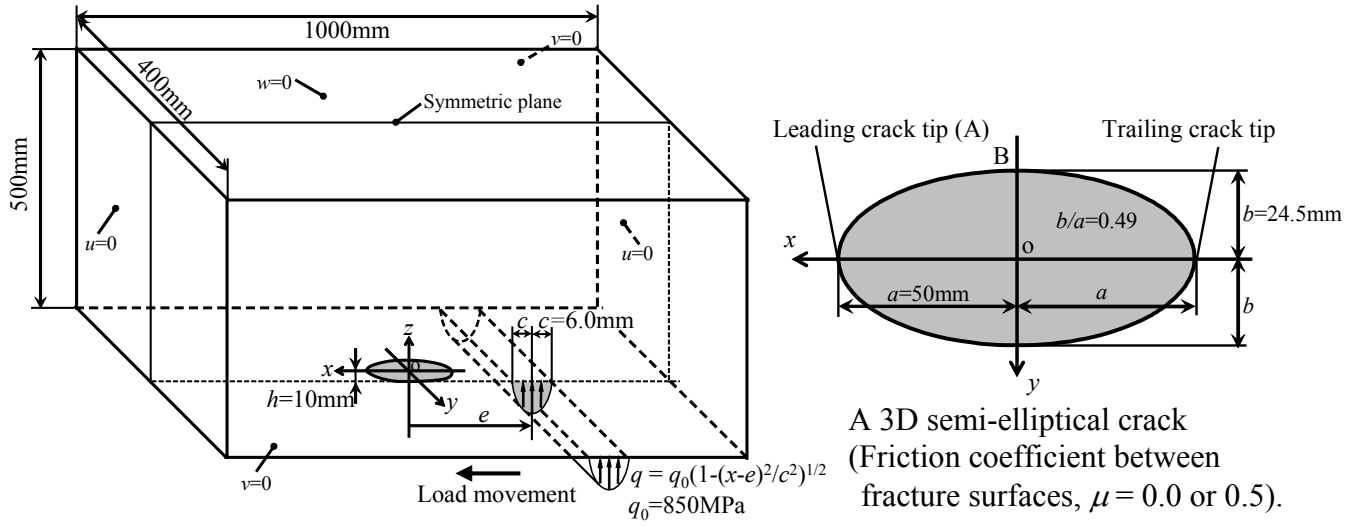

A 3D semi-elliptical crack (Friction coefficient between fracture surfaces, μ = 0.0 or 0.5).

Figure 11. FEM model and boundary condition (1/2 model).

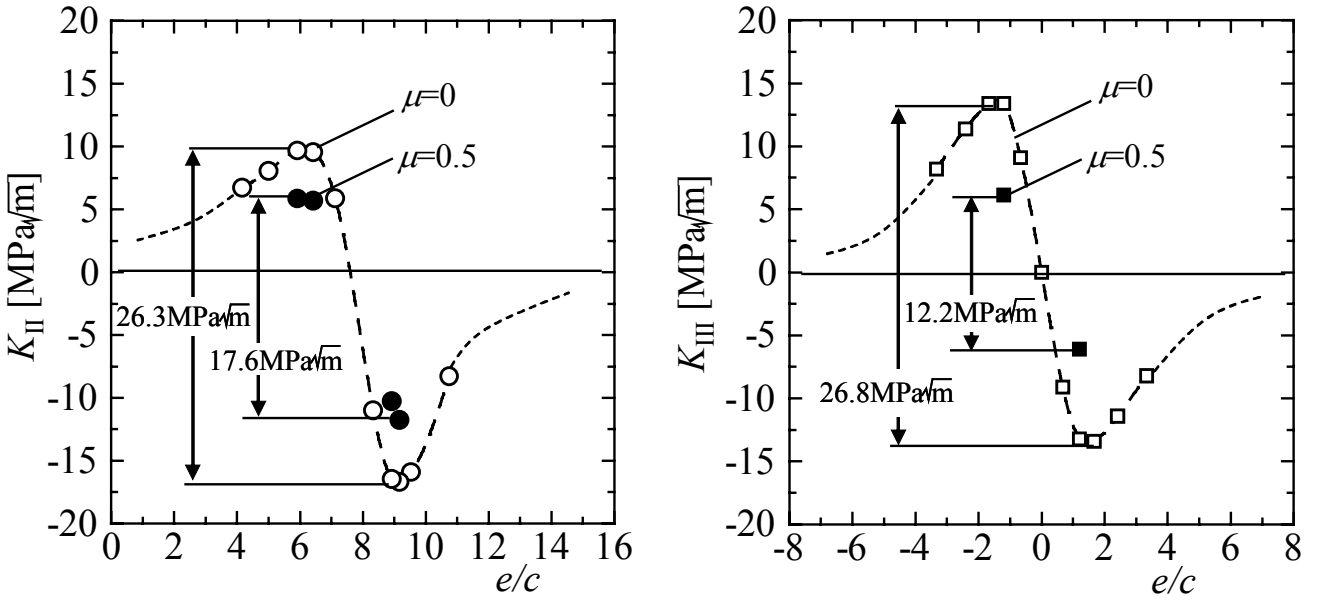

(a) K_{II} at the leading edge of the major axis of the elliptical crack.

(b) K_{III} at the edge of the minor axis of the elliptical crack.

Figure 12. Variation of the K_{II} at the leading edge of the major axis of the elliptical crack with the aspect ratio b/a = 0.49 (point A) and K_{III} at the edge of the minor axis of the elliptical crack with the aspect ratio b/a = 0.49 (point B).

CONCLUSIONS

(1) The crack in the reversed torsion of SAE52100 initiated from several slender MnS inclusions which are elongated in the longitudinal direction of a cylindrical specimen. The cracks first propagated up to the size of $2a$ = 100 ~ 200 μm (which are almost equal to the length of MnS inclusion) in the longitudinal direction by Mode II, and then branched by Mode I to the direction (~ ± 70.5 deg.) perpendicular to the local maximum normal stress ($\sigma_{\theta max}$) at the crack tip.

(2) The Mode II fatigue crack growth tests were conducted in air and in a vacuum. After ΔK_{II} reached the threshold value ΔK_{IIth}, the crack branched by Mode I. The branched angles of ± 70.5 deg. are the direction perpendicular to the local maximum normal stress ($\sigma_{\theta max}$). Fibrous pattern on the Mode II fatigue fracture surface tested in a vacuum was clearer than that in air due to the lack of oxidation.

(3) The Mode II threshold stress intensity factor ranges, ΔK_{IIth} = 10.2 MPa $\sqrt{m}$ (Longitudinal crack) and ΔK_{IIth} = 12.5 MPa $\sqrt{m}$ (Transverse crack) in a vacuum were higher than those in air, ΔK_{IIth} = 9.4 MPa $\sqrt{m}$ (Longitudinal crack) and ΔK_{IIth} = 10.8 MPa $\sqrt{m}$ (Transverse crack). Both in a vacuum and in air, the values of ΔK_{IIth} for crack growth perpendicular to the rolling direction were higher than those for crack growth parallel to the rolling direction.

(4) The 3D crack analysis shows that the most stable aspect ratio *b/a* of a small planar elliptical crack under cyclic shear stress is *b/a* = 0.49 in absence of friction at crack surfaces. The aspect ratio *b/a* = 0.49 can be explained by the equal resistance against fatigue crack growth both in Mode II and Mode III, i.e. $\Delta K_{IIth} = \Delta K_{IIIth}$. However, the aspect ratio *b/a* for the failure of a real railway did not stay at *b/a* = 0.49 and continued decreasing. Thus, the aspect ratio smaller than 0.49 can be attributed to the friction between crack surfaces.

APPENDIX

Crack propagation path from the edge of an elliptical hole under shear stress [17]

Figure 14 (a) and (b) show the crack path from an elliptical hole with the aspect ratio *b/a* = 0.5 and 0.2 under shear stress. We assume the initial crack initiates based on the local maximum stress criterion, the angle of the crack initiation is ± 45 deg. at the periphery of the ellipse where a 45 deg. inclined line contacts. The angle of the crack propagation once increases as the crack length increases, and then the angle decreases to ± 45 deg. again.

Figure 15 shows the relationship between the maximum angle θ_{max} during crack propagation and the aspect ratio *b/a* for the elliptical hole. For the aspect ratio *b/a* = 1 (Circular hole), the maximum angle θ_{max} is ± 45 deg.. However, as the aspect ratio *b/a* decreases to 0 (Crack), the maximum angle θ_{max} increases to ± 70.5 deg.. The crack growth length $l_{\theta max}/\alpha$ at the maximum angle θ_{max} decreases to zero as the aspect ratio *b/a* becomes zero (See Fig. 16). In the limiting case of a crack (*b/a* = 0), the crack growth length in the direction of ± 45 deg. is zero, resulting the actual crack branching angle to be ± 70.5 deg.. Thus, there is no theoretical contradiction in the initial crack propagation direction between a slender ellipse (± 45 deg.) and a crack (± 70.5 deg.).

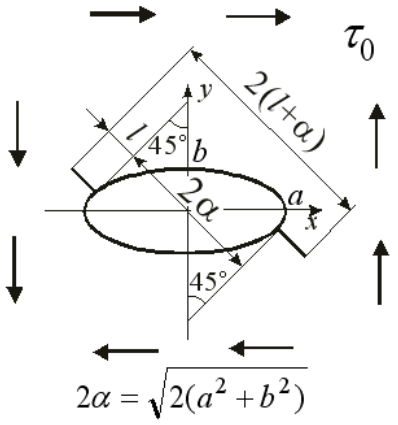

Figure 13. Definition of the length of the crack emanating from an elliptical hole under shear.

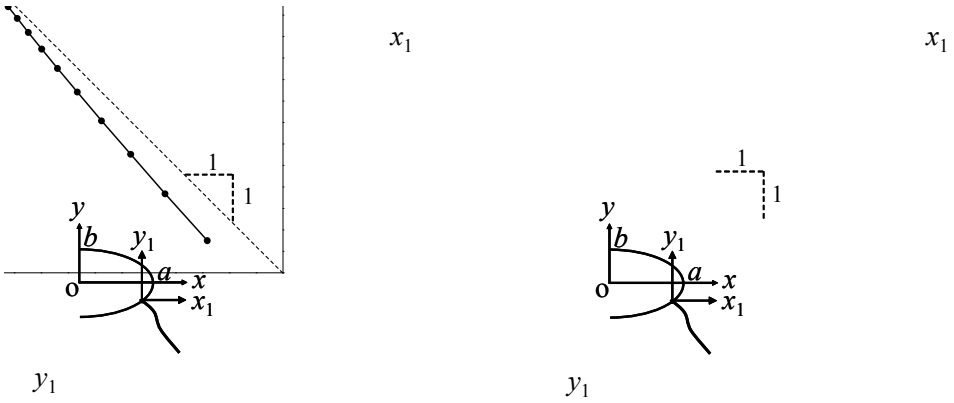

(a) $a = 1$, $b = 0.5$, $b/a = 0.5$. (b) $a = 1$, $b = 0.2$, $b/a = 0.2$.

Fig. 14 Crack propagation path from the edge of elliptical hole under shear stress [17].

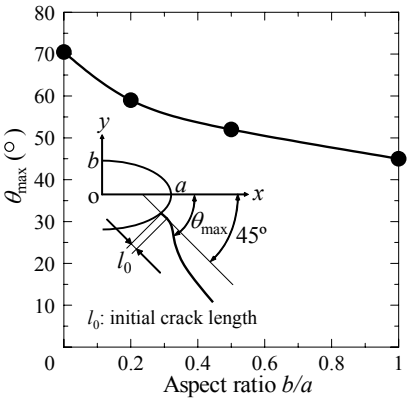

Fig. 15 Relationship between θ_{max} and aspect ratio b/a for elliptical holes [17].

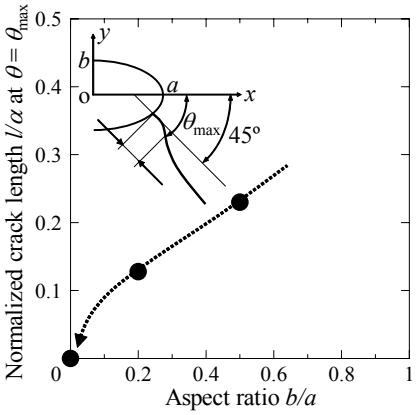

Fig. 16 Relationship between the crack length l/α at $\theta = \theta_{max}$ and aspect ratio b/a for elliptical holes [17].

REFERENCES

1. Grinberg, N. M., International Journal of Fatigue, Vol. 4, No.2, pp. 83-95 (1982).
2. Kikukawa, M., Jono, M. and Adachi, M., Journal of the Society of Materials Science, Japan, Vol. 27, No. 300, pp. 853-858 (1978).
3. Jono, M., Song, J. and Ohgaki, M., Transactions of the Japan Society of Mechanical Engineers, Series A, Vol. 51, No. 463, pp. 806-813 (1985).
4. McEvily, A. J. and Gonzalez Velazquez, J. L., Metallurgical Transactions A, Vol. 23A, pp. 2211-2221 (1992).
5. Nakamura, T., Kaneko, M., Kazami, S. and Noguchi, T., Journal of the Society of Materials Science, Japan, Vol. 49, No. 10, pp. 1148-1154 (2000).
6. Murakami, Y., Hamada, S., Sugino, K. and Takao, K., Journal of the Society of Materials Science, Japan, Vol. 43, No. 493, pp. 1264-1270 (1994).
7. Murakami, Y. and Hamada, S., Fatigue & Fracture of Engineering Materials & Structures, Vol. 20, No. 6, pp. 863-870 (1997).
8. Murakami, Y., Sakae, C. and Hamada, S., Engineering Against Fatigue, pp. 473-485 (1999) (Edited by Baynon, J. H., Brown, M. W., Lindley, T. C., Smith, R. A. and Tomkins, B.), A. A. Balkema, Rotterdam.
9. Murakami, Y. and Takahashi, K., Fatigue & Fracture of Engineering Materials & Structures, Vol. 21, No. 12, pp. 1473-1484 (1998).
10. Murakami, Y., Takahashi, K. and Kusumoto, R., Fatigue & Fracture of Engineering Materials & Structures, Vol. 26, No. 6, pp. 523-531 (2003).
11. Murakami, Y., Kusumoto, R. and Takahashi, K., Proceedings of the 14th European Conference on Fracture – ECF14, Vol. 2, pp. 493-500 (2002) EMAS publishing.
12. Toyama, K., Takahashi, K. and Murakami, Y., Proceedings of the International Conference on Advanced Technology in Experimental Mechanics – ATEM'03, CD-ROM, paper No. OS12 W0373 (2003).
13. Murakami, Y. and Natsume, H. International Journal of the Japan Society of Mechanical Engineers, Series A, Vol. 45, pp. 161-169 (2002).
14. Erdogan, F. and Sih, G. C., Transaction of the American Society of Mechanical Engineers, Journal of Basic Engineering, Vol. 85, pp. 519-527 (1963).
15. Kassir, M. K. and Sih, G. C., Transaction of the American Society of Mechanical Engineers, Journal of Applied Mechanics, Vol.33, pp. 601-611 (1966). In: Murakami, Y., Editor-in-chief, "Stress Intensity Factors Handbook", Vol. 2, p.686 (1987) Pergamon Press.
16. Beretta, S., Donzella, G., Roberti, R. and Ghidini, A., Proceedings of the 13th European Conference on Fracture – ECF13, CD-ROM, paper No. 3R. 147 (2000).
17. Kanezaki, T., Nagata, K. and Murakami, Y., Transactions of the Japan Society of Mechanical Engineers, Japan, Series A, Vol. 71, No. 711, pp. 1538-1545 (2005).